UNIVERSITÉ LAVAL

Widely tunable silicon Raman laser

Mohammad Ahmadi, Wei Shi, and Sophie LaRochelle

OSA Optica, (Accepted May 5, 2021)

Widely tunable silicon Raman laser

Mohammad Ahmadi, Wei Shi, Member, IEEE and Sophie LaRochelle* Fellow, IEEE, Fellow, OSA

Department of Electrical and computer Engineering, Centre d'optique, photonique et laser, Université Laval, Québec, Canada.
**sophie.larochelle@gel.ulaval.ca*

Abstract: Stimulated Raman scattering is an effective means of wavelength conversion and can largely extend the operating spectral range of an optical source. We demonstrate a high-performance tunable Raman laser on a sub-micrometer-thick silicon on insulator wafer using a standard foundry process. The key feature to this laser is the use of a tunable coupling mechanism to adjust both pump and signal coupling coefficients in the ring cavity, allowing demonstration of laser emission over a large wavelength tuning range of 83 nm. This Raman laser demonstrates efficient (slope of up to 26% and a maximum pump-to-signal power conversion efficiency of 10%) on-chip non-linear wavelength conversion. Our results indicate great promise for substantially increasing the optical spectral resources available on a silicon chip.

1. Introduction

Recent advances in silicon photonics (SiPh) have spurred interest for applications of photonic integrated circuits in a variety of fields. Robust fabrication methods have increased the effectiveness of the sub-micrometer silicon on insulator (SOI) wafers as an integrated photonics platform. Designers can now rely on libraries of validated passive and active building blocks, such as wavelength multiplexers, ring resonators, modulators, and photodetectors. Consequently, over the last decade, silicon photonics has become an enabling technology of various fields spanning from telecommunication to medicine [1-3].

A crucial component of photonic circuits and systems is the light source. Integrating lasers in SiPh circuits remains to this day an important challenge because silicon is characterized by an indirect band gap. In group IV materials, such as silicon, light emission is thus a phonon-assisted phenomenon, which is highly inefficient. To overcome this issue, the band structure of the gain medium must be engineered to enhance radiation, for example by using nanocrystals (Si-ns) or silicon quantum dots, alloys, and so on [4,5]. Various research efforts have therefore been undertaken to proposed solutions for SiPh on-chip laser sources. Excluding the use of external lasers, current integration approaches include group III-V lasers and optically pumped lasers [2,4]. High performance group III-V materials (InP, GaAs etc.) can be co-integrated with silicon wafer. These materials can be heterogeneously bonded on silicon layer by various techniques such as flip-chips, wafer bonding, and transfer printing, etc, or can be monolithically integrated by direct crystal growth on silicon layer [4-6].

In optically pumped on-chip lasers, a pump light is coupled to the chip from an external source, or generated via the techniques described above. For example, the gain medium can be a glass cladding layer with rare-earth doping, such as thulium or holmium [7,8]. Frequency conversion through nonlinear effects in silicon waveguides is another approach to on-chip light generation that can be achieved without any post processing of the SiPh chip. For example, in silicon, the third-order nonlinearity enables comb generation [9], supercontinuum generation [10], optical parametric oscillation [11], and Raman emission [12,13]. Among the available nonlinear effects, stimulated Raman-Stokes scattering (SRSS) can be advantageously used for wavelength conversion since it does not require phase matching. The silicon Raman gain has

National Science and Engineering Research Council of Canada (NSERC) Funding: STPGP 494358

therefore been exploited in various designs and models of on-chip lasers and amplifiers [14–27]. On-chip Raman lasers and amplifiers use simple cavity designs and have so far been achieved mostly with relatively thick silicon wafers [20,21].

In this work, we experimentally demonstrate a Raman laser on a sub-micrometer SOI wafer using a standard foundry process. Moreover, the proposed Raman laser is tunable over a large wavelength range, capable of converting pump wavelengths covering the band of 1530 nm to 1600 nm to output laser wavelengths spanning from 1662 nm to 1745 nm. The laser has a ring cavity surrounded by a *p-i-n* junction to remove free carrier and lower the loss. The key feature of this laser is a tunable directional coupler that allows the optimization of both pump and signal coupling coefficient in the cavity. Adjustment of these parameters is critical to achieve high performance over a wide wavelength range. This design is based on a comprehensive model and optimization method that we reported in [12] and the results demonstrate the interest of this design process to address the development of Raman lasers in other wavelength bands, such as the mid-infrared. The remainder of the paper is organized as follows: in Section 2, we describe the structure of the laser device, cavity parameters, and adjustable directional coupler characterization. Section 3 discusses the experimental setup and presents the characterization of the tunable Raman lasers. In addition, we discuss laser characteristics such as the threshold power, slope efficiency, and maximum input power. We present our conclusion in Section 4.

2. Tunable Raman laser design

Raman lasers in SiPh have been studied extensively [12-27], but few experimental demonstrations have been achieved since the seminal work of Rong *et al.* reporting a SiPh Raman laser with a ring cavity [15]. To improve the laser efficiency, Rong *et al.* added a *p-i-n* junction around the around the cavity waveguide, which reduces the free-carrier absorption loss. The threshold power was ~20 mW and the output power reached up to 50 mW (with input pump power of 300 mW) at a laser wavelength of λ_s=1686 nm (for a pump wavelength of λ_p=1550 nm). This result was later followed by a demonstration of a cascaded Raman laser with two output wavelengths: λ_s=1686 nm and λ_s=1848 nm [19]. They also presented a Fabry-Perot-cavity Raman laser with 12 nm tunablilty range, 280 mW threshold power and 4.3% slope efficiency. These SiPh Raman lasers were fabricated on wafers with a silicon layer thickness of H=1.55 μm. Raman laser was also demonstrated using silicon photonic crystal nanocavities targeting a strong light-matter interaction to increase Raman gain. Designing such a high quality factor nanocavity for Raman laser yielded a miniaturized device with an ultralow lasing threshold of 1 μW and output power close to 130 nW [26].

More recently, Y. Zhang *et al.* [27] reported a Raman laser on sub-micrometer silicon thickness (H=220 nm) SOI wafer, which is a more usual SOI layer for multi-project runs. In this work, the cavity is a multimode ring-resonator surrounded by *p-i-n* junctions. They examined their Raman laser at two wavelengths of 1440.5 nm and 1649 nm and reported the following results: the threshold power ~ 1.3 mW with a slope efficiency of only 1.4% and a maximum output power limited to ~0.03 mW at λ_s=1440.5 nm. They also reported an almost similar results at λ_s= 1649 nm.

The schematic of the proposed ring-cavity Raman laser in this study, with a cavity length of 3.5 mm, is shown in Fig. 1. The waveguide frame of reference (x y z) axis is placed at 45º with respect to the crystallographic axis of silicon ($\hat{x}$ $\hat{y}$ $\hat{z}$) fabricated on the (100) plane of the SOI substrate This waveguide orientation angle provides the maximum possible Raman gain to the laser which is obtained when a TE pump converts to a TE signal in counter-propagating configuration [22]. The laser cavity is a ring resonator, which has been shown to be more efficient than a Fabry-Perrot one [25]. To reduce the nonlinear loss associated with the

National Science and Engineering Research Council of Canada (NSERC) Funding: STPGP 494358

generated free carriers, a *p-i-n* junction is present around the waveguide (Fig. 1 (a)). Applying a reverse bias voltage helps to extract the generated free carriers from the active effective area of the waveguides and reduces carrier lifetime [12].

This laser was designed using a comprehensive model presented in [12]. This work investigates, through numerical simulations, taking into account silicon material properties, including gain and loss, as well as waveguide and cavity designs. Included in the model are propagation loss as well as losses due to two-photon absorption and free carrier absorption. Results show the importance of tuning both signal, κ^2_s, and pump, κ^2_p, power coupling ratio for optimal operation of the laser (power coupling ratios are the fraction of the pump and signal power that are cross-coupled in and out of the ring cavity). This optimum operation point depends on specific material and waveguide properties, such as loss, for which we only have an estimate at the time of the design. Therefore, a key aspect of the present design is to introduce a tunable coupler in the laser design, As discussed in [12, 28, 29], this approach provides a coupler that enables adjustment of the power coupling ratios in order to obtain the optimum set (κ^2_s, κ^2_p) for the signal and pump wavelengths. In the present case, the modeling was done assuming a worst case propagation loss of 2 dB/cm, a free carrier lifetime of 1 ns and a cavity length of 3.5 mm. Other parameters were estimated from the literature and theoretical analysis as discussed in [12]. The model predicted a maximum output of ~0.3 mW with 100 mW of input pump power, which turned out to be underestimated by one order of magnitude due to the lower propagation loss value (1.1 dB/cm) that results in a measured output power reaching 3.5 mW as will be discussed below in section 3.2.

As discussed above, the design of an adjustable directional coupler (DC) for the ring resonator cavity plays a fundamental role in achieving a robust, fabrication tolerant, and wavelength tunable device. The adjustable DC is made of a short Mach-Zehnder interferometric (MZI) structure built with two short (35.6 μm) directional couplers (the waveguide bend radius was 35 μm). The presence of a thermal element on the top of one arm, as shown in Fig. 1 (a), allows to trim and tune the power coupling ratios, which can maximize the output power for specific pump and signal output wavelengths. Figure 1 (b) shows the cross-section of the short directional couplers with a gap of 460 nm between the two ridge waveguides with 220 nm height and 90 nm slab thickness. The width of the intrinsic region of the p-i-n junction is 2.16 µm. Note that another thermal element is also placed on the top of the ring to tune the cavity resonance wavelength, which helps to align the cavity resonance to the laser frequency. The pump laser and the generated laser signal are counter propagating in the cavity and, therefore, the laser signals is retrieved at the input port of the pump laser.

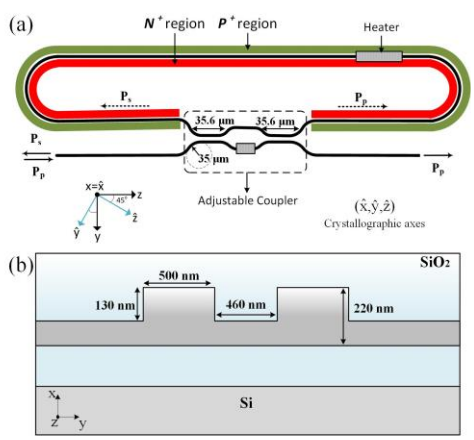

Fig. 1. (a) Schematic of the Raman laser with a ring-cavity of length 3.5 mm. The green and red regions represent the *p-i-n* junction. (b) Cross section of the DC.

National Science and Engineering Research Council of Canada (NSERC) Funding: STPGP 494358

3. Experimental Results

In this section, we present the experimentally measured performance of the SiPh tunable Raman laser fabricated at AMF in Singapore. We first characterize and calibrate the spectral transmission of the adjustable DC using a test structure. Then we extract propagation loss from spectral characterization of the passive cavity. The Raman laser output power and slope efficiency is investigated in details for pump (λ_p=1532 nm) and signal (λ_s=1665 nm). Finally, the tunable Raman laser emission over more than 83 nm (by 70 nm tuning of pump) is demonstrated.

3.1 Cavity characterization

Given the variations expected in SiPh fabrication, we first validated the operation of the tunable coupler to be able to target specific power coupling ratios during the Raman laser optimization. We then proceeded to determine the propagation loss in the cavity, which is an important parameter for precise modeling of the laser. Once propagation loss has been determined, we will be able to extract other unknown parameters, such as free carrier lifetime, by fitting the simulated results to the measured laser output as function pump power.

3.1.1 Adjustable DC

We characterized the power coupling ratios of the adjustable DC at both the pump and signal wavelengths (λ_p=1532 nm, λ_s=1665 nm) as a function of the electrical power applied to the thermal element. For this purpose, we used an adjustable DC test structure, which is similar to the adjustable DC of the laser in Fig. 1 (a) but has all input and output ports available for characterization, as depicted in Fig. 2 (a). Note that the laser signals are coupled in/out of the chip via edge couplers. We first launch the pump or signal laser at one input port of the adjustable DC test structure. Then, by applying a voltage on the thermal element, a phase difference is induced on one arm of the MZI, which shifts the spectral response of the device thereby tuning the transmission of the pump (signal). We thus swept the voltage applied to the thermal element and recorded the output power from P1 and P2 as shown in Fig. 2 (a). The current flowing in the thermal element was also measured in order to calculate the applied electrical power. The power coupling ratios therefore need to be extracted from the measured extinctions ratios using the relations presented in [30] and the results are shown in Fig. 2 (b). The adjustable DC provides values of pump and signal coupling ratios. We practically chose the optimum values by tuning the adjustable DC to maximize the laser output, which is the set of power coupling ratios (κ^2_p=0.21±0.03, κ^2_s=0.07±0.01) identified in Fig. 2 (b). The electrical power needed to set the target values of power coupling ratios in the laser cavity is thus obtained from this measurement although fine tuning is required as will be discussed in more detail in the next section.

National Science and Engineering Research Council of Canada (NSERC) Funding: STPGP 494358

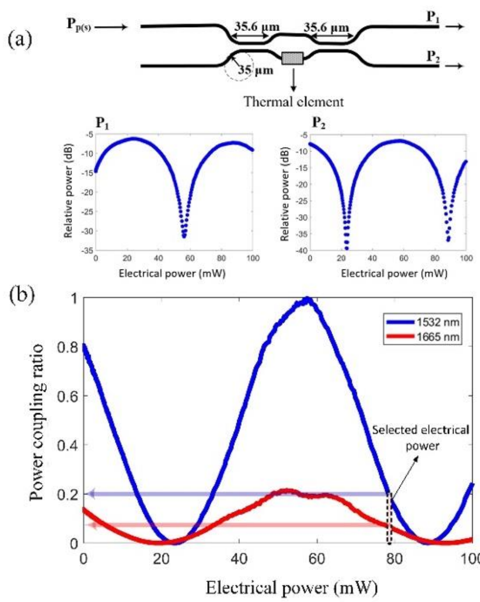

Fig. 2. (a) Schematics of the adjustable DC, P1 and P2 shows the output power of DC for different applied electrical power at λ=1532.2 nm. (b) Measurement of the cross-coupled power coupling ratio as a function of the electrical power applied to the thermal element. The optimized set of power coupling ratios (κ^2_p=0.21±0.03 and κ^2_s=0.07±0.01) are located at 79 mW.

3.1.2 Quality factor

To estimate the cavity loss from the loaded *Q*-factor, we measure the spectral transmission of the cavity resonance with a low pump power and 1.5 V reverse bias to the junction to reduce the free carrier absorption loss as much as possible from which we extract the loaded quality factor Q_{load} that is a function of both cavity loss and DC transmission. The intrinsic quality factor Q_{int} and cavity loss can then be determined using Eq. 1 and Eq. 2 below. A schematic of the measurement setup is presented in Fig. 3 (a), we used a tunable laser source (TLS) to sweep the wavelength with a precision of ~ 0.1 pm, and simultaneously recorded the output power of the cavity. The adjustable DC was tuned (by applying the electrical power to the thermal element) so as to bring the cavity transmission close to zero (T_0~0), which implies approaching the critical coupling regime at the pump wavelength [31], as shown in Fig. 3 (b). A Lorentzian curve is then fitted to the experimental result to determine Q_{load}, by which we find Q_{load} =3.5×10^5. The intrinsic quality factor Q_{int} is then calculated using:

$$Q_{\text{int.}} = \frac{2Q_{load.}}{1+\sqrt{T_0}} \tag{1}$$

where T_0 is the transmission at the cavity resonance, which gives Q_{int} =6.6×10^5 . Finally, the propagation loss can be estimated using

$$\alpha = \frac{2\pi\lambda_0}{Q_{\text{int.}} \times FSR \times L} \tag{2}$$

where L is the cavity length and FSR is the free spectral range of cavity [32]. The estimated propagation loss is α=1.1 dB/cm. We used this value in our numerical simulations to fit the experimental data.

National Science and Engineering Research Council of Canada (NSERC) Funding: STPGP 494358

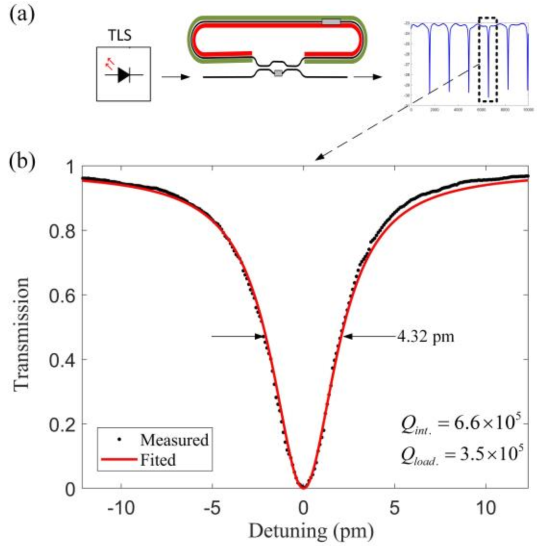

Fig. 3. (a) Q-factor measurement set-up. (b) The measured resonance spectrum of the ring-cavity (black dots) with FSR=0.167 nm and Lorentzian fit (red line), which gives the full-width at half maximum value of 4.32 pm at a wavelength of λ_p=1532 nm.

3.2 Laser output

A schematic of the experimental setup for testing the Raman laser is shown in Fig. 4. The pump laser is amplified by an erbium-doped fiber amplifier (EDFA), and a tap coupler is used to monitor the amplified pump power with a power meter. The polarization controller aids in launching TE-polarized light in the chip; both pump and signal are coupled in/out of the chip via edge couplers. The Raman laser signal is generated in the cavity in the counter propagating direction compared to the pump. The emitted signal is thus directed to the optical spectrum analyzer (OSA) by a circulator that captures the spectrum and measures the laser power. A weak signal was also observed at the other chip facet (co-propagating direction), which is attributed to the Fresnel reflection at the input chip-air interface and waveguide backscattering. Co-propagating laser operation is unlikely due to its large Raman effective area and was not observed in our simulations.

Since the cavity resonance of the ring resonator red-shifts during pump power injection in the cavity [27], we use a thermal element on the top of the cavity to control the cavity resonance. We heated the thermal element, injected the pump, and then gradually decreased the temperature of the element by lowering the voltage. Lowering the temperature blue-shifts the cavity resonance thereby eliminating the need to tune the pump wavelength (as proposed in [19,27]) as it is injected in the cavity. During the experiment, the power meter, on the right side of the schematic monitors the coupling condition of tapered fibers to the edge couplers, ensuring that the coupling remains optimized. To determine coupling efficiency, we measure the transmission of a straight waveguide test structure placed in close proximity to the laser cavity. We extract the coupling efficiency taking into account the propagation loss determined above. We find a coupling efficiency of ~ 33% at λ_p=1532nm and ~ 40 % at λ_s=1665 nm. In the results reported below, the losses of all components are thus calibrated out so that the pump power and signal power values are the ones present at input/output of the DC (left port in Fig. 1 (a)).

National Science and Engineering Research Council of Canada (NSERC) Funding: STPGP 494358

To operate the laser at the maximum possible output power, we first injected a high pump power (~ 70 mW) to the chip, then, an optimum pair of power coupling ratios (κ^2_p=0.21±0.03 and κ^2_s=0.075±0.01) was found by adjusting the DC and maximizing the output of the laser, as indicated in Fig. 2 (b). Then, the input pump power at λ_p=1532 nm was swept from 10 mW up to 80 mW, and the laser output at λ_s=1665 nm was measured. The results are displayed in Fig. 5 for two different reverse bias voltages, 1.5 V and 0.5 V, applied to the *p-i-n* junction. To set the reverse bias, we fixed the injected pump power near the maximum value and observed the Raman laser output. We did not observe any significant changes in the laser output when the reverse bias was larger than 1.5 V. This effect was simulated for a similar waveguide in [35], but for different in pump intensity, wavelength and width of the p-i-n intrinsic region. It shows an exponential decrease of the free carrier lifetime with reverse bias and, in our case, no further improvement was observed after 1.5 V. For the 1.5 V reverse bias, this experiment yields the following observations: pump power threshold, $P_{threshold}$= 15 ± 0.5 mW, slope efficiency ~ 26% (line slope between $P_{threshold}$ and P_{in}=18 mW), and maximum output power $P_{out\text{-}max}$= 3.7 ± 0.2 mW. The power conversion efficiency reaches a maximum of ~ 10% with a laser output power of ~ 3.5 mW obtained at an input pump power of ~35 mW. For future applications, the overall power efficiency of the Raman laser will depend on the chosen pump laser system that should be optimized for this purpose. At a reverse bias of 0.5 V, we obtained $P_{threshold}$= 16.25 ± 0.5 mW, slope efficiency ~ 17% (line slope between $P_{threshold}$ and P_{in}=21 mW), and $P_{out\text{-}max}$= 2.31± 0.1 mW. As expected, output power of laser increases as the reverse voltage applied to the *p-i-n* junction due to the lower free carrier absorption.

Fig. 5 shows that, with a 1.5 V reverse bias, the laser output power saturates when the input pump power reaches a value of ~35 mW. In the case of the 0.5 V reverse bias, the output power reaches a maximum, at approximately the same pump power, and then decreases. A possible explanation for this behavior, which is usually not taken into account in simulation models, is the fact that the carrier lifetime is a function of laser power [33], known as the screening effect [34]. This effect adds a nonlinear component to the free carrier absorption since the latter depends on the carrier lifetime. The screening effect is caused by charge accumulation in the waveguide that reduces the applied electric field. As observed in our experiment, and also simulated in [35], this effect results in a rapid increase of the free carrier lifetime after the pump intensity reaches a certain threshold. Numerical simulations of this effect are performed in [35] for waveguide dimensions of 500 x 200 x 50, for width, rib height, and slab height respectively, and with an intrinsic region width of 1.2 µm for the p-i-n junction. At 0 V reverse bias, it predicts that the screening effect becomes significant at a pump intensity of I~4×10^7 W/cm^2, which is agreement with our observation. Specifically, in our experiment, with a pump power of 35 mW and a cavity buildup factor ~3, the intensity is I~9×10^7 W/cm^2, which is in the range of intensity threshold of the screening effect depending on the bias voltage. Furthermore, in the case of the 0.5 V reverse bias, the higher nonlinear FCA loss translates to a quenching effect [24]. In other words, as more electrons build up in the waveguide with increased pump power, the increase in FCA loss becomes dominant over the increase in gain. Eventually, the electron-attributed loss becomes sufficiently large to overcome the Raman gain and stop the lasing.

National Science and Engineering Research Council of Canada (NSERC) Funding: STPGP 494358

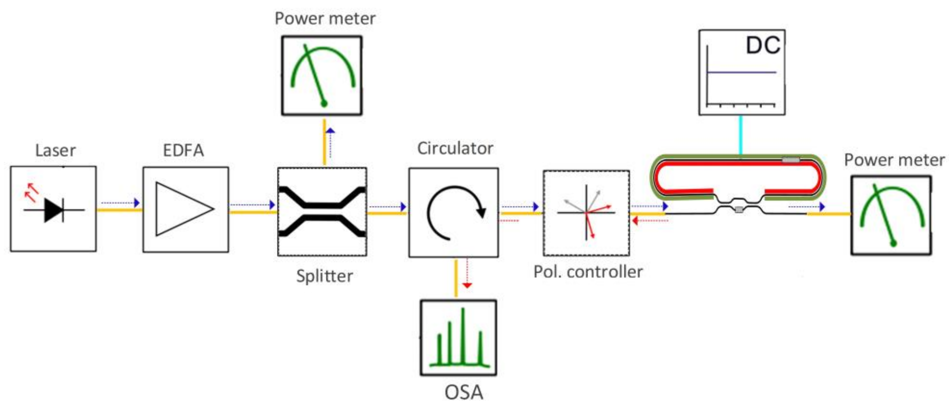

Fig. 4. Schematic of the Raman laser test setup. Blue line indicate electrical connections to the chip to apply electrical voltages to the *p-i-n* junction, thermal element of adjustable DC and thermal element for controlling the resonance of cavity. Yellow lines indicate optical fiber connections. The red dotted-arrows shows the Raman laser signal at 1665 nm directed to the OSA via the circulator, and the blue dotted-arrows shows the direction of the pump power at 1532 nm.

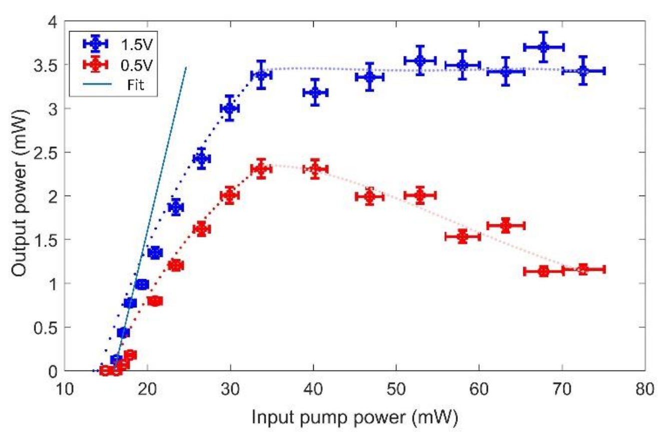

Fig. 5. The Raman laser output power at 1665 nm as a function of input pump power at 1532 nm for 1.5 V (blue dots) and 0.5 V (red dots) reverse bias. The blue line shows the linear regression fit between $P_{threshold}$ and P_{in}=18 mW giving a slope efficiency of 26%. Error bars show the uncertainty in the launched pump power and the measured Raman laser power. The dotted lines represent the simulated results. Lines with lighter color (above input pump power of 35 mW) indicate the range where the screening effect comes into play.

To characterize the free carrier lifetime for different pump powers, we used the model and simulation method presented in [12]. The parameters used in the simulations include the experimentally determined values of the propagation loss α=1.1 dB/cm (extracted from the *Q*-factor measurement), the calculated values of the Raman gain coefficient (g=9.62 cm/GW), and the two-photon absorption coefficients (β_{pp}=0.49 cm/GW, β_{ss}=0.26 cm/GW, β_{sp}= 0.36 cm/GW, where *p* and *s* represent the pump and signal [12]. To determine the best fit to the experimental data, we adjusted the power coupling ratios to κ^2_p=0.33 and κ^2_s=0.08, which are slightly different from the values κ^2_p=0.21±0.03 and κ^2_s=0.07±0.01 expected from the calibration of the test device at this electrical power. Such difference is not unexpected considering variations in the fabrication process and the fact that the test structure of the adjustable DC is located ~1 mm away from the laser cavity on the chip. This means that, although the layout of both devices are

National Science and Engineering Research Council of Canada (NSERC) Funding: STPGP 494358

the same, the power coupling ratios obtained for a given applied electrical power to the thermal tuner of the MZI can vary slightly in different areas of the chip.

A good fit between the simulations and experimental results was thus obtained by considering a constant carrier lifetime for low input pump power, i.e. 0.73 ns and 0.58 ns for reverse bias of 0.5 V and 1.5 V and pump power lower than 35 mW. For higher pump power, the carrier lifetimes extracted from the model by fitting the experimental results are shown in Fig. 6 for the two reverse bias voltages. Free carrier lifetime changes as a function of input power in Fig. 6 reveal the role of screening effect in our experiment. In agreement with numerically simulated results in [35], lifetime is constant in low pump powers then it gradually increase depending on the applied reverse bias. To further optimize the Raman laser performance, a possible approach would be to investigate the impact of the waveguide width on several important laser parameters, namely propagation loss, free carrier lifetime, Raman gain and nonlinear loss. Although a wider waveguide could be multimode, it is possible to excite only the fundamental mode using an adiabatically tapered waveguide as suggested in [27]. With a 2 μm wide waveguide, the laser could benefit from a lower propagation loss (down to 0.4 dB/cm [27]), allowing for a decrease in the laser threshold and improved power conversion efficiency. Currently, the model presented in [12] takes into account Raman gain and non-linear loss dependence on waveguide width, but does not consider dependence of the free carrier lifetime [36] and scattering loss [37].

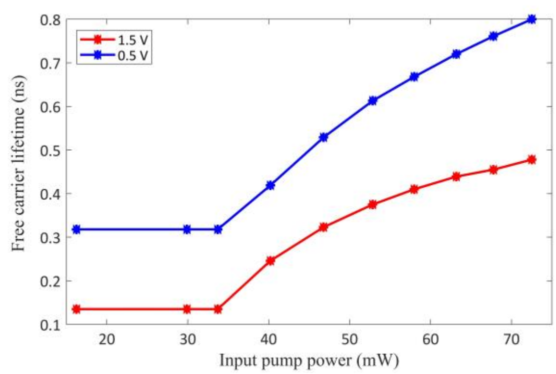

Fig. 6. Free carrier lifetime obtained from fitting the simulation results to experimental data as shown in Fig. 5. The Blue and red line-dots attribute to 0.5 V and 1.5 V reverse bias applied to *p-i-n* junction.

3.3 Tunable laser

We now present the tuning results of the laser. An important advantage of the proposed device is the possibility to adjust the power coupling ratios by fine tuning the electrical power applied to the DC and hence find the most optimal power coupling ratios that maximize the laser output. We used the same setup and technique to characterize the tunable laser as in Fig 4 above. The results measured with a reverse bias voltage of 1.5 V are shown in Fig. 7. We measured the laser performance with three different pump powers for each specific wavelength as presented in Fig. 7(a). The measured corresponding laser outputs are presented in the Fig. 7 (b). The laser output power for each specific wavelength almost remained constant by changing the attributed input pump power, which means the laser reached the plateau of saturation for the three input pump powers. The Raman laser output power is expected to decrease at longer wavelength as the gain coefficient scales $\propto 1/\lambda$ and the propagation loss will also be larger due to greater sidewall interaction. The measured optical spectra for three pump and Raman laser signal wavelengths are shown in Fig. 8.

National Science and Engineering Research Council of Canada (NSERC) Funding: STPGP 494358

In addition, we measured the linewidth of the Raman laser using the passive coherent discriminator method [38,39]. We determined the frequency noise spectral density of the Raman laser, and analyzed the low-frequency noises to extract the linewidth of the laser. At a laser signal wavelength of 1662 nm and 1703 nm, we estimated the linewidth to be < 12 MHz and <2.4 MHz, respectively. These values are dominated by EDFA noise, and thus, we expect the actual values to be smaller than these numbers with a cleaner pump.

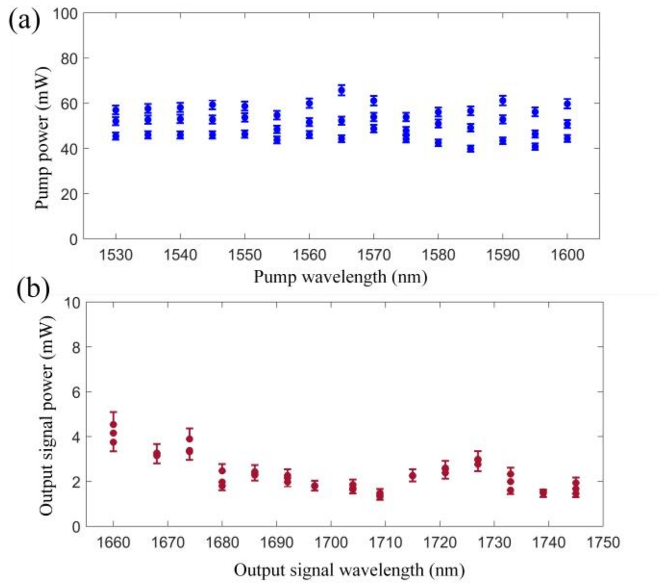

Fig. 7. (a) The three different pump powers for each of the pump wavelengths that range from 1530 nm to 1600 nm. (b) The corresponding Raman laser output signal power over the range from 1662 nm to 1745 nm. The experiment was carried out with 1.5 V reverse bias. Error bars show the uncertainty range for the input pump and output signal powers as determined by the small observed fluctuations of the input/output edge coupling.

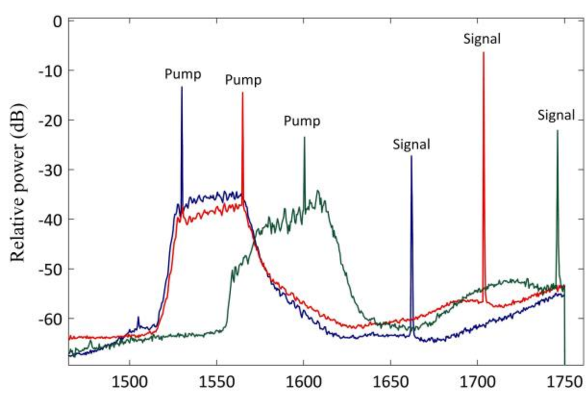

Fig. 8. Uncalibrated optical spectrum of the Raman laser output signal at 1662 nm, 1703 nm, and 1745 nm respectively. The signals are separated by 15.6 THz from the corresponding pumps at wavelengths of 1530 nm, 1565 nm, and 1600 nm. Some of the pump power reflected back to the OSA is also present on the spectrum.

National Science and Engineering Research Council of Canada (NSERC) Funding: STPGP 494358

4. Conclusion

In this study, we proposed a widely tunable Raman laser on a sub-micrometer SOI wafer. Our device uses a reconfigurable ring cavity with the capacity of tuning simultaneously the center wavelength and the coupling conditions of both the pump and signal for optical performance. The design led to the experimental demonstration of an efficient tunable silicon Raman laser with a slope-efficiency of up to 26% and a maximum pump-to-signal power conversion efficiency of 10%. The Raman conversion efficiency can be further improved by reducing the waveguide loss, e.g., by optimizing the fabrication process or waveguide geometry. The laser operation was fully characterized with cavity and coupler parameters extracted using test structures. We measured output laser power with respect to input pump power and compared the data with numerical simulation. Our results confirmed that the screening effect has a significant impact on the carrier lifetime at a high pump power, leading to output saturation. Multi-mill watt Raman laser emission has been achieved over an ultra-wide spectral range of 83 nm (from 1662 nm to 1745 nm). To the best of our knowledge, this is the first demonstration of a continuously and widely tunable Raman laser on a silicon chip. Our proposed structure can also be used for even longer wavelength conversion penetrating into the mid-IR region of the spectrum.

Funding. This work was supported, in part, by the Sentinel North program, a Canada First Excellence Research Fund initiative at Université Laval, and, in part, by the Natural Sciences and Engineering Research Council of Canada through a strategic project grant STPGP 494358. (Corresponding author: Sophie LaRochelle).

Acknowledgments. We thank Prof. J. Genest and V. Michaud-Belleau for their help and insights with the laser linewidth measurement. The authors acknowledge S. Levasseur, N. Landry, N. Bacon and P. Jean for their invaluable help in the laboratory and fruitful discussions.

Disclosures. The authors declare no conflicts of interest.

References

[1] L. Chrostowski, and M. Hochberg, *Silicon Photonics Design: from device to system*. (Cambridge University Press, 2015).

[2] B. Jalali, and S. Fathpour, "Silicon Photonics," J. Lightwave Technol. **24**(12), 4600-4615 (2006).

[3] Wei Shi, Ye Tian, and Antoine Gervais. "Scaling capacity of fiber-optic transmission systems via silicon photonics." Nanophotonics **9**(16), 4629-4633 (2020).

[4] J. C. Norman, , D. Jung, Z. Zhang, Y. Wan, S. Liu, C. Shang, R. W. Herrick, W. W. Chow, A. C. Gossard, and J. E. Bowers, "A review of high-performance quantum dot lasers on silicon," *IEEE J. Quantum Electron.* **55**(2), 1–11 (2019).

[5] Charles Cornet, Yoan Léger, Cédric Robert, *Integrated Lasers on Silicon*, (Elsevier: iSTE Press, 2016).

[6] Y. Hu, D. Liang, K. Mukherjee, Y. Li, C. Zhang, G. Kurczveil, X. Huang, and R. G. Beausoleil, "III/V-on-Si MQW lasers by using a novel photonic integration method of regrowth on a bonding template," Light Sci. Appl. **8**(1), 93 (2019).

[7] N. Li, P. Purnawirman, Z. Su, E. Salih Magden, P. T. Callahan, K. Shtyrkova, M. Xin, A. Ruocco, C. Baiocco, E. P. Ippen, F. X. Kärtner, J. D. Bradley, D. Vermeulen, and M. R. Watts, "High-power thulium lasers on a silicon photonics platform," Opt. Lett. **42**(6), 1181–1184 (2017).

[8] N. X. Li, E. S. Magden, Z. Su, N. Singh, A. Ruocco, M. Xin, M. Byrd, P. T. Callahan, J. D. B. Bradley, C. Baiocco, D. Vermeulen, and M. R. Watts, "Broadband 2-μm emission on silicon chips: monolithically integrated Holmium lasers," Opt. Express **26**(3), 2220–2230 (2018).

[9] A. G. Griffith, R. K. Lau, J. Cardenas, Y. Okawachi, A. Mohanty, R. Fain, Y. H. Lee, M. Yu, C. T. Phare, C. B. Poitras, A. L. Gaeta, and M. Lipson, "Silicon-chip mid-infrared frequency comb generation," Nat. Commun. **6**, 6299 (2015).

[10] R. Kou, T. Hatakeyama, J. Horng, J. H. Kang, Y. Wang, X. Zhang, and F. Wang, "Mid-IR broadband supercontinuum generation from a suspended silicon waveguide," Opt. Lett. **43**(6), 1387–1390 (2018).

[11] B. Kuyken, X. Liu, R. M. Osgood, R. Baets, G. Roelkens, and W. M. J. Green, "A silicon-based widely tunable short-wave infrared optical parametric oscillator," Opt. Express **21**(5), 5931–5940 (2013).

[12] M. Ahmadi, L. Bodiou, W. Shi, and S. Larochelle, "Comprehensive modeling and design of Raman lasers on SOI for mid-infrared Application," J. Light Technol. **38**(15), 4114–4123 (2020).

[13] Mohammad Ahmadi, Loïc Bordiu, Wei Shi, and Sophie Larochelle. "Design and modeling a mid infrared Raman laser on silicon-on-insulator," *In 2020 Photonics North (PN)*(2020), pp. 1-1.
[14] M. A. Ferrara, and L. Sirleto, “Integrated Raman laser: a review of the last two decades,” Micromachines **11**(3), 1–19 (2020).
[15] H. Rong, S. Xu, Y. Kuo, V. Sih, O. Cohen, O. Raday, and M. Paniccia, “Low-threshold continuous-wave Raman silicon laser,” Nat. Photonics **1**(4), 232–237 (2007).
[16] O. Boyraz, and B. Jalali, “Demonstration of a silicon Raman laser,” Opt. Express **12**(21), 5269–5273 (2004).
[17] H. Rong, A. Liu, R. Jones, O. Cohen, D. Hak, R. Nicolaescu, A. Fang, and M. Paniccia, “An all-silicon Raman laser,” Nature **433**(7023), 292–294 (2005).
[18] H. Rong, R. Jones, A. Liu, O. Cohen, D. Hak, A. Fang, and M. Paniccia, “A continuous-wave Raman silicon laser,” Nature **433**(7027), 725–728 (2005).
[19] H. Rong, S. Xu, O. Cohen, O. Raday, M. Lee, V. Sih, and M. Paniccia, “A cascaded silicon Raman laser,” Nat. Photonics **2**(3), 170–174 (2008).
[20] Yang, Xiaodong, and Chee Wei Wong. "All-silicon raman amplifiers and lasers based on micro ring resonators." U.S. Patent No. 7,532,656. (2009).
[21] B. Jalali, O. Boyraz, D. Dimitropoulos, and V. Raghunathan, “Silicon Raman laser, amplifier, and wavelength converter,” *Proc. SPIE*, **5840**, 16–28, (2005).
[22] F. De Leonardis, B. Troia, and V. M. N. Passaro, “Design rules for Raman lasers based on SOI racetrack resonators,” *IEEE Photonics J.* **5**(6), 1502431 (2013).
[23] V. Raghunathan, D. Borlaug, R. R. Rice, and B. Jalali, “Demonstration of a mid-infrared silicon Raman amplifier,” **15**(22), 1954–1956, (2007).
[24] M. Krause, “Efficient raman amplifiers and lasers in optical fibers and silicon waveguides: new concepts,” Ph.D. dissertation, Hamburg TU., Harburg, Germany, (2007).
[25] M. Krause, H. Renner, and E. Brinkmeyer, “Raman lasers in silicon photonic wires : unidirectional ring lasing versus Fabry-Perot lasing,”, Electron. Lett. **45**(1), 24–25 (2009).
[26] Y. Takahashi, Y. Inui, M. Chihara, T. Asano, R. Terawaki, and S. Noda,“ A micrometre-scale Raman silicon laser with a microwatt threshold,” Nature **498**(7455), 470–474 (2013).
[27] Y. Zhang, K. Zhong, and H. K. Tsang, “Raman lasing in multimode silicon racetrack resonators,” Laser Photonics Rev., **15**(2), 1–8 (2020).
[28] M. Tran, J. Hulme, S. Srinivasan, J. Peters, and J. Bowers, “Demonstration of a tunable broadband coupler,” Proc. IEEE Photon. Conf. (IPC), 488–489(2015).
[29] J. K. Doylend, O. Cohen, M. R. Lee, O. Raday, S. Xu, V. Sih, H. Rong, and M. Paniccia, “Tunable ring resonators for silicon Raman laser and amplifier applications,” Proc. SPIE **6896**, 68960Q (2008).
[30] M. A. Tran, T. Komljenovic, J. C. Hulme, M. L. Davenport, and J. E. Bowers, “A robust method for characterization of optical waveguides and couplers,” IEEE Photon. Technol. Lett. **28**(14), 1517–1520 (2016).
[31] W. Bogaerts, P. De Heyn, T. Van Vaerenbergh, K. De Vos, S. Kumar Selvaraja, T. Claes, P. Dumon, P. Bienstman, D. Van Thourhout, and R. Baets, “Silicon microring resonators,” Laser & Photon. Rev. **6**(1), 47–73 (2012).
[32] L. W. Luo, G. S. Wiederhecker, J. Cardenas, C. Poitras, and M. Lipson, “High quality factor etchless silicon photonic ring resonators,” Opt Express **19**(7), 6284–6289 (2011).
[33] I. Aldaya, A. Gil-Molina, J. L. Pita, L. H. Gabrielli, H. L. Fragnito, and P. Dainese, "Nonlinear carrier dynamics in silicon nano-waveguides," Optica **4**, 1219-1227 (2017).
[34] D. Dimitropoulos, S. Fathpour, and B. Jalali. "Limitations of active carrier removal in silicon Raman amplifiers and lasers," Appl. Phys. Lett. **87**(26), 261108 (2005).
[35] A. Gajda, L. Zimmermann, J. Bruns, B. Tillack, and K. Petermann, “Design rules for p-i-n diode carriers sweeping in nano-rib waveguides on SOI,” Opt. Express **19**(10), 9915–9922 (2011).
[36] D. Dimitropoulos, R. Jhaveri, R. Claps, J. C. S. Woo, and B. Jalali , “Lifetime of photogenerated carriers in silicon-on-insulator rib waveguides ,” Appl. Phys. Lett. **86**, 071115 (2005).
[37] A. Delâge, B. A. Syrett, B. Lamontagne, J. Lapointe, J. H. Schmid, K. P. Yap, P. Waldron, and S. Janz, “Correlation of Scattering Loss, Sidewall Roughness and Waveguide Width in Silicon-on-Insulator (SOI) Ridge Waveguides,” J. Light. Technol. **27**(18), 3999–4008 (2009).
[38] V. Michaud-Belleau, H. Bergeron, P. S. Light, N. B. Hébert, J. D. Deschênes, A. N. Luiten, and J. Genest. "Passive coherent discriminator using phase diversity for the simultaneous measurement of frequency noise and intensity noise of a continuous-wave laser." Metrologia, **53**(5), 1154(2016).
[39] G. Di Domenico, S. Schilt, and P. Thomann, “Simple approach to the relation between laser frequency noise and laser line shape,” Appl. Opt. **49**(25), 4801–4807 (2010).

National Science and Engineering Research Council of Canada (NSERC) Funding: STPGP 494358